Journal of Materials Chemistry A

PAPER

View Article Online
View Journal | View Issue

Cite this: J. Mater. Chem. A, 2014, 2, 692

A simple approach for PtNi–MWCNT hybrid nanostructures as high performance electrocatalysts for the oxygen reduction reaction

Shangfeng Du,*[a] Yaxiang Lu,[a] Sairam K. Malladi,[b] Qiang Xu[b] and Robert Steinberger-Wilckens[a]

Received 9th September 2013
Accepted 29th October 2013

DOI: 10.1039/c3ta13608f

www.rsc.org/MaterialsA

We report a simple one-pot synthesis of PtNi–MWCNT hybrid nanostructures as a high performance and durable electrocatalyst for the oxygen reduction reaction (ORR) in polymer electrolyte fuel cells (PEFCs). The whole approach was achieved in aqueous solution at room temperature, without using any organic solvents, templates or growth inducing catalysts. A single-crystal Pt nanoparticle was successfully grown on Ni nanoparticle surfaces using commercial Ni-coated MWCNTs as a support. PtNi–MWCNT hybrids possessed a high mass activity of 0.51 A mg_{Pt}^{-1}, nearly double that of the state-of-the-art TKK's Pt/C catalyst. After an accelerated durability test by 2500 potential sweeping cycles, PtNi–MWCNTs still retained 89.6% of their initial mass activity, which is 0.46 A mg_{Pt}^{-1} and 4% higher than the DOE (Department of Energy) target of 0.44 A mg_{Pt}^{-1} for 2017–2020. The reported synergy between high performance and simple synthesis demonstrated that PtNi–MWCNTs could be effective cathode catalysts for high performance PEFCs.

Introduction

Benefiting from the high energy efficiency and low carbon emission, polymer electrolyte fuel cells (PEFCs) have been considered as the prime candidate for power to portable and transportation applications, but the high cost and poor durability still remain as big challenges for their development and applications.[1] Among several components in PEFCs, the high performance cathode electrocatalysts for the oxygen reduction reaction (ORR) play a key role in the overall PEFC performance since the majority of activation losses occur at the cathode.[2,3] Carbon supported platinum (Pt) nanoparticles (Pt/C) are typically utilized as the ORR catalyst but are inadequate to fulfill the combined cost, performance, and durability requirements. To promote the development of highly active ORR catalysts, the United States Department of Energy (DOE) sets the mass activity target of 0.44 A mg^{-1} for 2017–2020.[4]

Previous studies have established that the activity of the ORR catalysts could be improved by using bimetallic catalysts which tentatively enhance the performance and prevent the degradation of the Pt catalyst.[5] Following this concept, studies have shown that the PtNi alloyed nanoparticles exhibit ORR specific activity 10 times greater than that of Pt.[6] On volcano plots, the $Pt_3Ni(111)$ alloy could potentially provide the highest ORR activity among the Pt and early transition metal alloy, due to the optimum binding energy of O on the surface.[5] Remarkable progress toward fundamental understanding of ORR activity has motivated recent research in developing highly active PtNi alloy nanoparticles with sizes of practical relevance.[4,7–10] However, the long-term stability of these alloyed nanoparticles is strongly affected by metal segregation and de-alloying. Furthermore, the complex preparation process of the catalyst is neither rigorous nor has the market-price targets for mass production yet been satisfied.

On the other hand, the catalyst support plays an important role in distributing and stabilizing the catalyst particles, as well as in the diffusion kinetics of the reactants and products in the catalytic system.[2,11] Recent observations suggest that some new carbon-based support materials, *e.g.* carbon nanotubes (CNTs), can offer beneficial interactions between catalyst and support which substantially enhance catalyst activity and stability.[12] Multi-walled carbon nanotubes (MWCNTs) are one class of materials that can be used to promote better utilization of the Pt catalyst, compared to the traditional carbon black materials. This is due to their morphology and some interesting properties such as nanometer size, highly or easily accessible surface area, good thermal and chemical stability, as well as high electrical conductivity. There are different methods for dispersing Pt on CNTs. However, the tubular shape of CNTs, consisting of interconnected stable hydrophobic carbon atoms, offers a poor surface to host metal particles. This chemically inert feature of CNTs makes a uniform Pt dispersion adhere to them a challenge, and their surface functionalization by chemical oxidation

[a]School of Chemical Engineering, University of Birmingham, Edgbaston, Birmingham B15 2TT, UK. E-mail: s.du@bham.ac.uk
[b]Kavli Institute of Nanoscience, Delft University of Technology, Lorentzweg 1, 2628 CJ, Delft, The Netherlands

is usually essential.[13] This functionalization can help achieve good nanoparticle dispersion, but, the good mechanical and electronic properties of CNTs are usually also altered.[2] Furthermore, the added functionalization step, to some degree, brings extra cost in the preparation of catalysts and more unreliability to catalysts themselves. Therefore, by a low cost and reliable process, the synthesis of a new type of high-quality PtNi–MWCNT as a high-efficiency ORR catalyst is highly desirable and technologically important.

Here, we demonstrate, for the first time, a simple one-pot synthesis of PtNi–MWCNT hybrid nanostructures. The approach has two important benefits. (i) A single-crystal Pt nanoparticle was grown directly on the Ni nanoparticle surface using commercially available nickel-coated MWCNTs, without using any surfactants; the corresponding hybrids exhibited much higher electrochemical activity and stability towards the ORR than the state-of-the-art Pt/C catalysts (TKK TEC10E50E, 45.9 wt % Pt on high surface area carbon). (ii) The whole growth process was achieved by using formic acid (HCOOH) as a reductant at room temperature in aqueous solution, without heating or adding any other organic or poisonous reductants such as ethylene glycol, hydrazine, dimethylhydrazine, hydroquinone, *etc.*

Experimental section

Synthesis of PtNi–MWCNT hybrids

Nickel-coated MWCNTs (US Research Nanomaterials Inc, $599/25g), with a purity >98%, 60 wt% Ni and 38 wt% MWCNTs, were used as a support. To grow Pt nanoparticles on the surface, the Ni–MWCNTs were dispersed in water to form a dispersion of 10 g L^{-1} by sonication horn for 10 min (130 W, 40% amplitude). In a typical process, the as-prepared Ni–MWCNT dispersion (0.8 mL), 31.8 mg chloroplatinic acid hexahydrate (Sigma-Aldrich UK, ACS reagent) and 1 mL formic acid (Sigma-Aldrich UK, ACS reagent) were mixed in pure water to form an aqueous solution (20 mL). The mixture was then left for reaction at room temperature. After 72 hours, the deposition was washed with water and collected by centrifugation. The final product was dispersed in water to form 2 mL dispersion for further characterization.

Physical characterization

The as-prepared PtNi–MWCNT hybrids were characterized using a field emission scanning electron microscope (FE-SEM, JEOL 7000F, operating at 20 kV). High-resolution transmission electron microscopy (HR-TEM) images were recorded on a FEI Tecnai F20ST microscope operating at 200 kV. X-Ray diffraction (XRD) patterns were obtained with a Siemens 5005 X-ray diffractometer using Cu Kα radiation at $\lambda = 1.5418$ Å. X-Ray photoelectron spectroscopy (XPS) characterization was performed on an XPS spectrometer (AXIS Nova, Kratos Analytical) by using high power monochromatized Al Kα radiation (1486.6 eV). XPS spectra were fitted using CasaXPS V2.3.16 software in which a Shirley background was assumed, and fitting the peaks of the experimental spectra was completed by considering a combination of Gaussian (90%) and Lorentzian (10%) distributions.

Electrochemical measurements

All electrochemical experiments were performed at 298 K in a standard three-electrode system, using an Autolab PGSTAT302N potentiostat and a glassy carbon rotating disc electrode (RDE, a geometric area of 0.196 cm^2) setup (ED101, Radiometer Analytical). The background electrolyte was 0.1 M $HClO_4$, prepared from 70% (AR, Fisher), purged with N_2 gas for at least 20 minutes before testing. Potentials are recorded against the RHE (reversible hydrogen electrode) and the counter electrode was a platinum mesh attached to a platinum wire. Ultra-pure water (18.2 MΩ, Millipore) was used throughout. To prepare the working electrode, all catalyst samples were diluted to 0.4 μg μL^{-1} (based on Pt mass) by using water, iso-propanol (IPA) and 10 wt% Nafion aqueous solution with a ratio of water–IPA–Nafion solution of 3 : 1 : 0.02. 10 μL of the dispersion was transferred onto the RDE. The loading amount of Pt for all catalysts was 4 μg. The working electrodes were dried overnight at 40 °C in a vacuum oven.

The working electrode was first activated using cyclic voltammetry (CV) between 0.05 V and 1.1 V with a scan rate of 100 mV s^{-1} in N_2-purged 0.1 M $HClO_4$ solution until a steady CV was obtained. CV curves were conducted between 0.05 V and 1.1 V with a scan rate of 20 mV s^{-1}. The electrochemical surface area (ECSA) was estimated by measuring the charges associated with hydrogen desorption (Q) between 0.05 and 0.40 V after double-layer correction and assuming a value of 210 μC cm^{-2} for the adsorption of a monolayer of hydrogen onto a Pt surface (q_H).[14] The ORR measurements were conducted by a linear sweep voltammetry technique in O_2 (BOC, 99.999%) saturated 0.1 M $HClO_4$ solutions using the glassy carbon RDE with rotation speeds from 400 to 2000 rpm at a sweep rate of 20 mV s^{-1}. The kinetic current was calculated from LSV curves after ohmic drop (IRs) correction based on the Koutecky–Levich equation:

$$1/i = 1/i_k + 1/i_d \quad (1)$$

where i is the experimentally measured current, i_d is the diffusion-limiting current, and i_k is the kinetic current. The ohmic drop correction was done by subtracting the IR to the applied potential, where the electrolyte resistance (R_s) value was obtained by electrochemical impedance spectroscopy (EIS) for each electrode. The EIS measurement was performed in oxygen saturated 0.1 M $HClO_4$ solution between 10 kHz and 1 Hz with an amplitude of 5 mV. For each catalyst, the kinetic current was normalized to ECSA in order to obtain specific area activities. The electrochemical stabilities of the catalysts were also investigated by the accelerated durability tests (ADT), which were carried out in O_2-saturated 0.1 M $HClO_4$ solutions by applying 2500 cyclic potential sweeps between 0.6 and 1.1 V *vs.* RHE at a sweep rate of 50 mV s^{-1}.

Results and discussion

The commercial Ni-coated MWCNTs were used as purchased without further treatment. According to the supplier, the Ni nanoparticles were deposited by a chemical vapor deposition (CVD) technique, and the MWCNTs have an inside diameter of

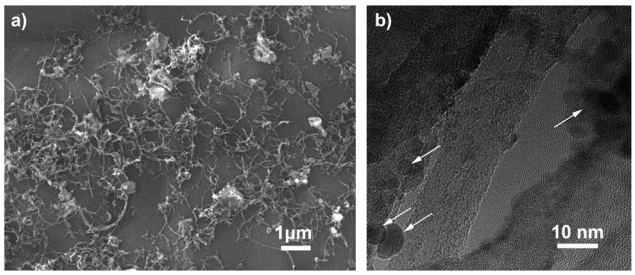

Fig. 1 SEM and BF-TEM images of Ni–MWCNTs. The arrows in the TEM image show the presence of non-uniform clusters of Ni nanocrystals and the aggregates over the inert surface of MWCNTs.

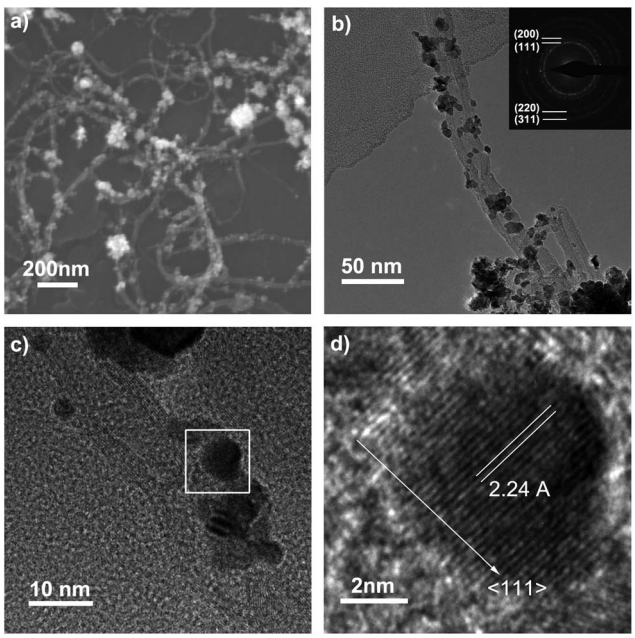

Fig. 2 (a) SEM and (b) BF-TEM images of PtNi–MWCNTs. The inset in image (b) shows the corresponding diffraction pattern. (c) and (d) show high resolution TEM images of PtNi–MWCNTs. Image (d) taken from the white square in image (c) shows one of the single Pt nanocrystal revealing the 2.24 Å $\{111\}_{Pt}$ lattice fringes.

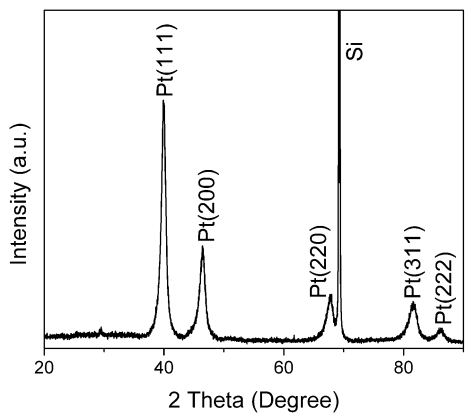

Fig. 3 XRD pattern of PtNi–MWCNTs. The strong peak at 2θ of 69.35° came from the silicone substrate used.

3–5 nm, an outside diameter of 5–15 nm and a length of *ca.* 50 μm. SEM and Bright Field TEM (BF-TEM) images are shown in Fig. 1. The MWCNTs have a wall of *ca.* 10–20 layers, with some Ni nanoparticles deposited along the surface. The Ni nanoparticles have a size of 2–6 nm, but some of them grow to very large aggregates of several hundred nanometers. The distribution of Ni nanoparticles is non-uniform on the MWCNT surface. This may be due to the inert surface property of MWCNTs as mentioned previously.

Fig. 2 shows the SEM and BF-TEM images of Pt nanoparticles grown on Ni–MWCNTs. It can be seen that some Pt nanoparticles grow over the MWCNT surface, while some of them

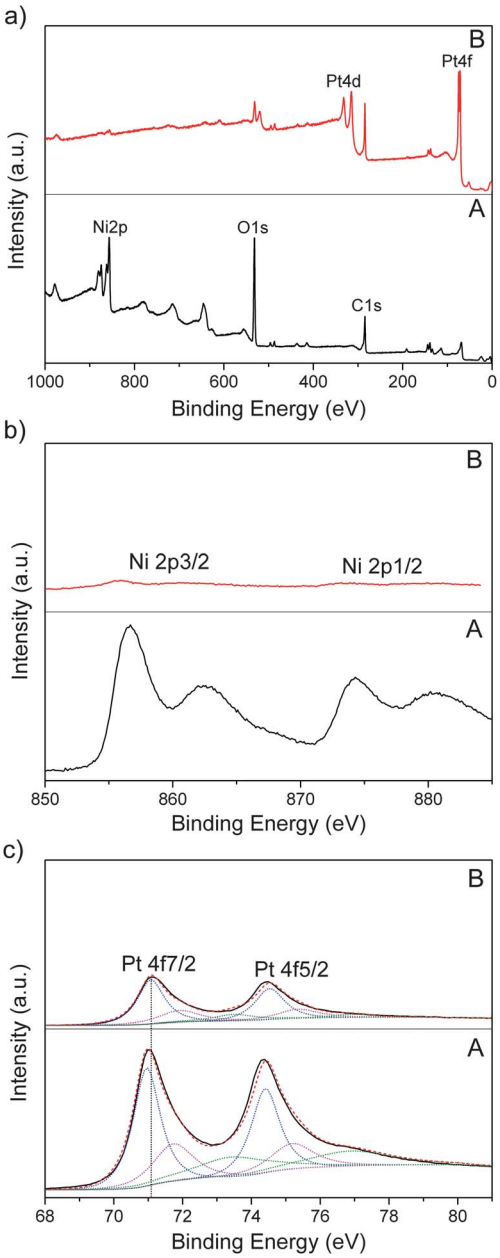

Fig. 4 (a and b) XPS survey and Ni 2p patterns of Ni–MWCNTs (A) and PtNi–MWCNTs (B); (c) Pt 4f pattern comparison of PtNi–MWCNTs (B) with Pt black (A).

tend to form large aggregates similar to Ni nanoparticles as shown in Fig. 1. Fig. 2b shows a BF-TEM image along with the corresponding diffraction pattern in the inset showing the aggregates of Pt nanocrystals. Fig. 2c shows a high-resolution TEM image of Pt nanoparticles over MWCNTs. Fig. 2d (taking from white square area in Fig. 2c) reveals that the particle is a single crystal with the lattice spacing between the planes of 0.224 nm, which is in agreement with the value {111} facets of a bulk Pt crystal.[15] The XRD analysis (Fig. 3) indicates a good crystallization of the Pt nanoparticles. The main peaks were well indexed to a face-centered-cubic (fcc) structure similar to bulk Pt.

To characterize the Pt nanoparticles grown on Ni–MWCNTs, XPS analysis was performed. The patterns are presented in Fig. 4. The XPS survey pattern in Fig. 4a shows a comparison of Ni–MWCNTs before and after Pt growth. After the growth of Pt nanoparticles, the signal from Ni 2p, as further shown in the binding energy range from 850 eV to 885 eV in Fig. 4b, became extremely low, while the Pt signals, specified by Pt 4f and Pt 4d peaks at around 75 eV and 315 eV, respectively, showed a very strong intensity. The significant decrease of Ni signals and the strong Pt signals indicated that Pt nanoparticles covered nearly the entire Ni nanoparticle surface on the MWCNTs, which results in a hybrid nanostructure of Pt nanoparticles as shell covering the Ni nanoparticle core. The covering of Ni by Pt resulted in a very weak Ni peak. In fact, the inert surface feature of MWCNTs, consisting of the interconnected stable hydrophobic carbon atoms, means a much larger nucleation energy barrier must be overcome for Pt nanoparticles to grow directly on the surface of a MWCNT, as compared to the Ni nanoparticle surface, resulting in a preferred growth of Pt on the Ni surface. This is also the reason why a surface functional process is necessary for depositing Pt on a CNT surface, as mentioned before. On the other hand, the selected growth of Pt on Ni nanoparticle surfaces specifies that the non-uniform Ni nanoparticles and their large aggregates on MWCNT surfaces would result in quite a similar particle size distribution to Pt nanoparticles; this is consistent with the results shown in Fig. 1 and 2. According to previous research, the Pt 4f peak position of PtNi hybrids should have a slight shift in the XPS pattern due to the special interaction effect at the interface between Pt and Ni as compared to bulk Pt. In our case, we observed this shift, but it is much smaller than those reported in the literature on PtNi alloyed nanoparticles[7,10,16] where the total nanoparticle structure has been changed due to the metal alloy. Fig. 4c shows a comparison between the Pt 4f peaks of the PtNi–MWCNTs and a commercial Pt black sample (Johnson-Matthey HiSPEC™ 1000). A peak shift of 0.1 eV was observed for Pt 4f peaks.

The ECSA of catalysts was determined during CV in N_2 saturated 0.1 M $HClO_4$ electrolyte with a scan rate of 20 mV s^{-1} (Fig. 5a). The results were compared with the state-of-the-art TKK Pt/C catalyst with 45.9 wt% Pt supported on high surface area carbon. On a Pt mass basis, PtNi–MWCNTs and Pt/C had ECSA values of 47.9 and 128.6 m^2 g^{-1}, respectively. The commercial Pt/C catalyst has an average particle size of around 2–3 nm,[17] which is smaller than that of the as-prepared PtNi–MWCNTs (as shown in Fig. 2). This large Pt particle size in PtNi–MWCNTs finally resulted in a much smaller ECSA value. CV scan was also performed for the support Ni–MWCNTs to check their influence on the whole catalyst. The result indicated an extremely small activity of Ni–MWCNTs. Electrochemical impedance spectra (EIS) at 0.90 V of the three samples are

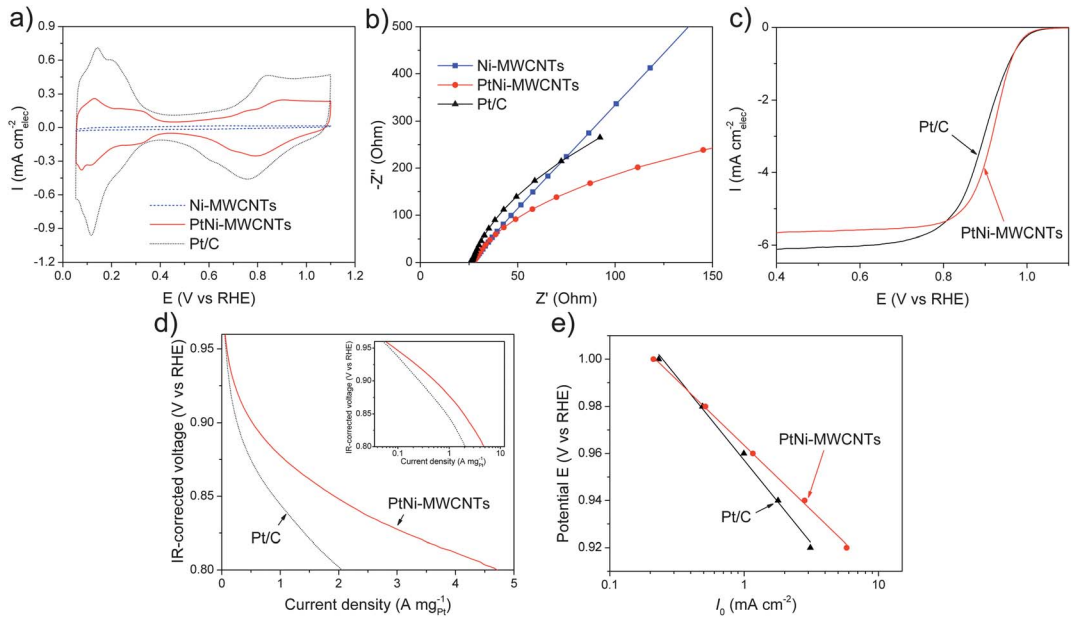

Fig. 5 (a) CV of Ni–MWCNTs, PtNi–MWCNTs and TKK Pt/C, recorded in N_2 saturated 0.1 M $HClO_4$ solution with a scan rate of 20 mV s^{-1}; (b) electrochemical impedance spectra (EIS) collected at 0.9 V in O_2 saturated 0.1 M $HClO_4$; and ORR activities of PtNi–MWCNTs and TKK Pt/C measured with linear sweep voltammetry at 1600 rpm (c), kinetic activities (d) and Tafel plots (e). Inset in (d): details of the same figure but with the *x*-axis in logarithmic scale.

shown in Fig. 5b. A very large polarization resistance was also obtained for the support Ni–MWCNTs. Consequently, the contribution of the support to the ORR activity could be ignored in this discussion. PtNi–MWCNTs exhibited a smaller polarization resistance than TKK Pt/C, indicating a possible higher ORR activity. This difference in the ORR activity was further examined with RDE experiments by the linear sweep voltammetry (LSV) with rotating speed from 400 rpm to 2000 rpm. Fig. 5c and d show the polarization curves of two catalysts recorded at a rotating speed of 1600 rpm and the related kinetic activities. The kinetic activity was evaluated according to eqn (1) by taking the measured current at 0.9 V *vs.* RHE during the linear sweep voltammetry after an IR correction (Fig. 5b). The catalyst activity for ORR was normalized to the total Pt mass. PtNi–MWCNTs produced a Pt mass activity of 0.51 A mg_{Pt}^{-1}, 16% greater than the DOE target of 0.44 A mg_{Pt}^{-1},[4] and nearly double that of the Pt/C catalyst, 0.26 A mg_{Pt}^{-1}. Catalysts were also evaluated in terms of specific area activity. Of particular interest was the large area activity of PtNi–MWCNTs, 1.07 mA cm^{-2}, exceeding the Pt/C (0.24 mA cm^{-2}) by a factor of 4.2. The Tafel plots at the high potential range for two catalysts are shown in Fig. 5e. The exchange current density was obtained from the intercept at the current density axis from the Koutecky–Levich plots calculated from LSV at different rotating speeds. The slope was a bit lower for PtNi–MWCNTs compared with TKK Pt/C, which were 54 mV per decade and 63.1 mV per decade, respectively. This smaller Tafel slope of PtNi–MWCNTs is in line with the better kinetic activity as shown in Fig. 5b–d. The Tafel slope of TKK Pt/C obtained here was quite close to that of pure Pt.[2] PtNi–MWCNT hybrids showed a slightly higher slope than those for the PtNi alloy or core–shell structures.[2,18] This large slope was possibly caused by the simple assembly of Pt and Ni individual nanoparticles in the hybrid structures, which was different from that in alloy or core–shell structures where two types of atoms were really kept in one crystal. This point on hybrid structure for PtNi–MWCNTs is in coincidence with the TEM and XPS results discussed above.

Accelerated durability tests (ADT) were conducted by cycling potential sweeps at 50 mV s^{-1} between 0.6 and 1.1 V *vs.* RHE, with ECSA and ORR measurements taken after cycling (Fig. 6). PtNi–MWCNTs and Pt/C retained 86.4% and 54.6% of their original ECSAs, respectively, after 2500 cycles (Fig. 6a and b). PtNi–MWCNTs showed a significant durability improvement to Pt/C, attributed to the single crystal feature of Pt nanoparticles, the synergistic effect between Pt and Ni, and the MWCNT support reducing Pt degradation and loss. The mass activities were determined following durability testing (Fig. 6c). Following 2500 cycles, the mass activity of PtNi–MWCNTs and Pt/C degraded to 0.46 and 0.20 A mg_{Pt}^{-1}, retaining 89.6% and 75.2% of their original value, respectively. PtNi–MWCNTs still produced an ORR mass activity of 3.8% higher than the DOE target of 0.44 A mg_{Pt}^{-1}.

A comparison of the ORR activity of the as-prepared PtNi–MWCNT hybrids and other related bi-metallic electrocatalysts from the literature is listed in Table 1. It can be seen that our PtNi–MWCNTs exhibited a quite competitive performance, in particular by such a simple and scalable process. It is worthwhile to say that the higher activity and stability in electrochemical performance observed here can probably be attributed to three major factors: (i) electronic tuning, due to the synergistic effect between Pt and Ni at the interface of the PtNi hybrids,[16,19] potentially contributed to the high ORR activity. The Ni support alloying with the Pt layer at the interface introduces compressive strain, widening the Pt d-band and shifting the centre further from the Fermi level, as shown in XPS by Pt 4f shifting in Fig. 4c; the d-band center shift weakened oxygen chemisorption, improving ORR activity;[2,20] (ii) the single crystal feature of Pt nanoparticles enables them to have a high stability compared to the amorphous structure which has an increased surface energy; furthermore, it enables the exposure

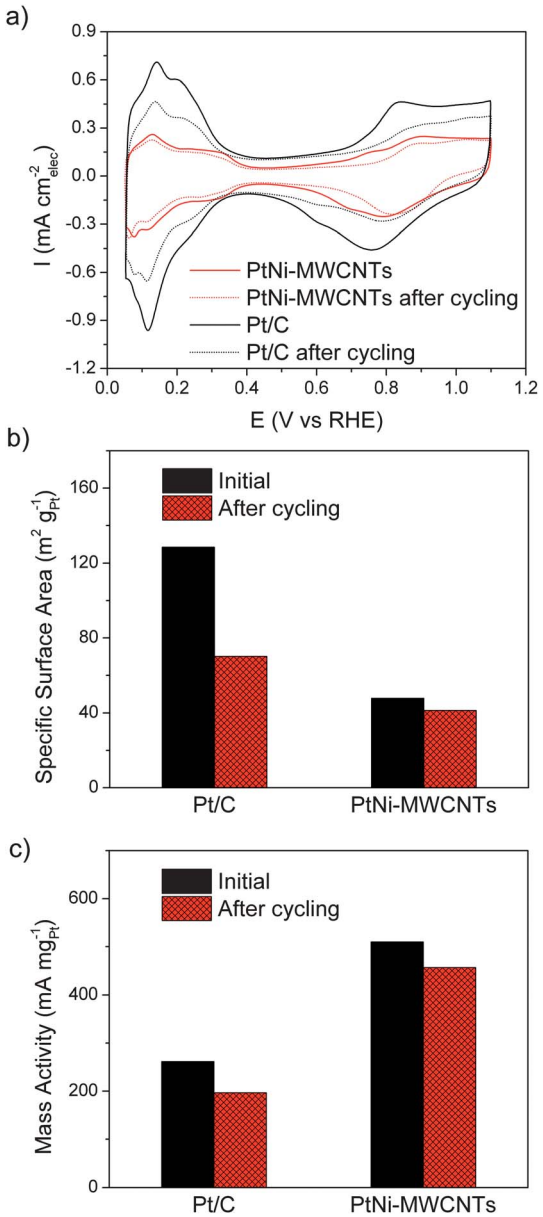

Fig. 6 CV (a), summary of the specific surface area (b) and mass activities (c) of the catalysts before and after the potential cycling. The mass activities were normalized by the initial loading of Pt metal.

Table 1 ORR activity of typical Pt related bi-metallic electrocatalysts

Electrocatalyst		Mass activity (A mg^{-1})	Specific activity (mA cm^{-2})	Reference
Pt–Ni	Hybrid PtNi–MWCNTs	0.51	1.065	This work
	$Pt_{56}Ni_{44}$/C	0.17	0.69	Loukrakpam *et al.*[35]
	Core–shell PtNi@Pt	0.03	0.13	Li *et al.*[36]
	De-alloyed $PtNi_3$	0.29	1.49	Hasche *et al.*[37]
	PtNi hollow nanoparticles	0.50	1.5	Bae *et al.*[38]
	Core–shell PtNiN	0.86	1.65	Kuttiyiel *et al.*[39]
	Octahedral $Pt_{2.5}Ni$/C	3.3	7.0	Choi *et al.*[40]
Pt–Pd	Pd–Pt nanodentrites	0.24	0.8	Lim *et al.*[41]
	Pd_3Pt_1/NMCC	0.15	Not given	Li *et al.*[42]
	Pt–Pd_9 Au nanowires	2.08	0.95	Koenigsmann *et al.*[43]
	Pt-coated Pd nanotubes	1.8	1.0	Alia *et al.*[44]
Pt–Co	$Pt_{73}Co_{27}$/C	0.33	0.45	Loukrakpam *et al.*[35]
	$Pt_{20}Co_{80}$/C	0.24	0.41	Jayasayee *et al.*[45]
Pt–Cu	$Pt_{75}Cu_{25}$/C	0.21	0.43	Jayasayee *et al.*[45]
	Core–shell PtCu	0.49	0.55	Marcu *et al.*[46]
	Skeleton PtCu	0.51	0.60	Marcu *et al.*[46]
Pt–Au	PtAu nanoparticles	0.03	1.74	Park *et al.*[47]
Pt–Fe	PtFe nanowires	0.08	Not given	Zhang *et al.*[48]

of the (111) facet of the single-crystal Pt nanoparticles on the Ni nanoparticle surface. According to the research, the (111) facet is believed to constitute the active facet of the Pt nanoparticles which catalyze the ORR, thus a high electrochemical activity is as expected;[21–25] (iii) the higher chemical stability of MWCNTs as compared with carbon in commercial Pt/C catalysts, reducing catalyst degradation and loss.[12,13] Another point that should be mentioned here is the role of Ni in Pt growth. As we know, with formic acid as reductant for synthesizing Pt nanostructures at room temperature, the usual products obtained are Pt nanowires. This synthesis process is dominated by the enhanced anisotropic growth of Pt along the ⟨111⟩ direction due to the very low reduction rate at room temperature.[26] This mechanism has been demonstrated in water[27] or on carbon-based supports, *e.g.* carbon black,[28] carbon fibres,[29] carbon paper,[30,31] as well as carbon nanotubes.[32] Here the Ni nanoparticles coated on the MWCNT surface should partially play a role as a growth inducing catalyst, decreasing the nucleation and growth energy, enhancing the reduction rate and Pt nanoparticles were finally formed. In fact, the utilization of Ni as a growth inducing catalyst for CNTs[33] and ZnO[34] has been reported previously, but the situation is different here. Further work needs to be done to understand the real growth mechanism.

Conclusions

PtNi–MWCNT hybrid catalysts have been synthesized by a simple one-pot process and have significantly higher activities towards the oxygen reduction reaction (ORR) than the state-of-the-art TKK Pt/C. The specific and mass activities are 1.065 mA cm^{-2} and 0.51 A $mg_{Pt}{}^{-1}$, respectively, The high mass activity allowed PtNi–MWCNTs to surpass the DOE mass activity target of 0.44 A mg^{-1}, while expressing an electrochemical surface area (ECSA) of only 47.9 m^2 g^{-1}. PtNi–MWCNTs further retained a greater proportion of ECSA and ORR activity than Pt/C after durability test: 86.4% and 89.6% following 2500 potential sweeping cycles, respectively, particularly noteworthy because of the use of the Ni–MWCNT substrate, the selective exposure of Pt (111) facets and the synergistic effect in PtNi hybrid nanostructures. The use of commercially available support is cost-effective although only the non-uniform Ni nanoparticles have been coated on surfaces; the simple one-pot synthesis in aqueous solution at room temperature is a significant benefit from the prospective production and can potentially make a larger impact on the commercialization of PEFCs.

Acknowledgements

This work was supported by the FCH JU project TriSOFC (303454). Y. X. Lu was sponsored by a joint Li Siguang Scholarship from the University of Birmingham and the China Scholarship Council. X-ray photoelectron spectra were obtained at the National EPSRC XPS User's Service (NEXUS) at Newcastle University, an EPSRC Mid-Range Facility.

References

1 The Fuel Cell Industry Review 2012, in *Platinum Met. Rev.*, 2012, **56**, 272–273.
2 J. Zhang, *PEM fuel cell electrocatalysts and catalyst layers: fundamentals and applications*, Springer, London, 2008.
3 K. W. Guo, *Int. J. Energy Res.*, 2012, **36**, 1–17.
4 D. Papageorgopoulos, *DOE hydrogen and fuel cells program: FY*, 2012, annual progress report.
5 J. Greeley, I. E. L. Stephens, A. S. Bondarenko, T. P. Johansson, H. A. Hansen, T. F. Jaramillo, J. Rossmeisl, I. Chorkendorff and J. K. Norskov, *Nat. Chem.*, 2009, **1**, 552–556.
6 V. R. Stamenkovic, B. Fowler, B. S. Mun, G. F. Wang, P. N. Ross, C. A. Lucas and N. M. Markovic, *Science*, 2007, **315**, 493–497.

7 M. C. Elvington and H. R. Colon-Mercado, *Electrochem. Solid-State Lett.*, 2012, **15**, K19–K22.
8 J. L. Shui, J. W. Zhang and J. C. M. Li, *J. Mater. Chem.*, 2011, **21**, 6225–6229.
9 H. Li, H. Lin, Y. Hu, H. X. Li, P. Li and X. G. Zhou, *J. Mater. Chem.*, 2011, **21**, 18447–18453.
10 T. Ghosh, B. M. Leonard, Q. Zhou and F. J. DiSalvo, *Chem. Mater.*, 2010, **22**, 2190–2202.
11 W. Chaikittisilp, K. Ariga and Y. Yamauchi, *J. Mater. Chem. A*, 2013, **1**, 14–19.
12 L. B. Hu, D. S. Hecht and G. Gruner, *Chem. Rev.*, 2010, **110**, 5790–5844.
13 P. Luksirikul, K. Tedsree, M. G. Moloney, M. L. H. Green and S. C. E. Tsang, *Angew. Chem., Int. Ed.*, 2012, **51**, 6998–7001.
14 S. Trasatti and O. A. Petrii, *Pure Appl. Chem.*, 1991, **63**, 711–734.
15 S. F. Du and B. G. Pollet, *Int. J. Hydrogen Energy*, 2012, **37**, 17892–17898.
16 A. L. M. Reddy, S. R. Gowda, M. M. Shaijumon and P. M. Ajayan, *Adv. Mater.*, 2012, **24**, 5045–5064.
17 Y. Shao-Horn, W. C. Sheng, S. Chen, P. J. Ferreira, E. F. Holby and D. Morgan, *Top. Catal.*, 2007, **46**, 285–305.
18 U. A. Paulus, A. Wokaun, G. G. Scherer, T. J. Schmidt, V. Stamenkovic, V. Radmilovic, N. M. Markovic and P. N. Ross, *J. Phys. Chem. B*, 2002, **106**, 4181–4191.
19 X. Ding, Y. Zou, F. Ye, J. Yang and J. Jiang, *J. Mater. Chem. A*, 2013, **1**, 11880–11886.
20 D. He, Y. Jiang, H. Lv, M. Pan and S. Mu, *Appl. Catal., B*, 2013, **132–133**, 379–388.
21 J. C. Meier, I. Katsounaros, C. Galeano, H. J. Bongard, A. A. Topalov, A. Kostka, A. Karschin, F. Schuth and K. J. J. Mayrhofer, *Energy Environ. Sci.*, 2012, **5**, 9319–9330.
22 J. N. Tiwari, R. N. Tiwari and K. S. Kim, *Prog. Mater. Sci.*, 2012, **57**, 724–803.
23 J. A. Keith, G. Jerkiewicz and T. Jacob, *ChemPhysChem*, 2010, **11**, 2779–2794.
24 J. Greeley, J. Rossmeisl, A. Hellman and J. K. Norskov, *Z. Phys. Chem.*, 2007, **221**, 1209–1220.
25 A. S. Bondarenko, I. E. L. Stephens, H. A. Hansen, F. J. Perez-Alonso, V. Tripkovic, T. P. Johansson, J. Rossmeisl, J. K. Norskov and I. Chorkendorff, *Langmuir*, 2011, **27**, 2058–2066.
26 S. Du, *Int. J. Low-Carbon Technol.*, 2012, **7**, 44–54.
27 S. H. Sun, G. X. Zhang, D. S. Geng, Y. G. Chen, R. Y. Li, M. Cai and X. L. Sun, *Angew. Chem., Int. Ed.*, 2011, **50**, 422–426.
28 S. H. Sun, F. Jaouen and J. P. Dodelet, *Adv. Mater.*, 2008, **20**, 3900–3904.
29 S. H. Sun, D. Q. Yang, D. Villers, G. X. Zhang, E. Sacher and J. P. Dodelet, *Adv. Mater.*, 2008, **20**, 571–574.
30 S. F. Du, *J. Power Sources*, 2010, **195**, 289–292.
31 S. F. Du, B. Millington and B. G. Pollet, *Int. J. Hydrogen Energy*, 2011, **36**, 4386–4393.
32 S. Sun, D. Yang, G. Zhang, E. Sacher and J. P. Dodelet, *Chem. Mater.*, 2007, **19**, 6376–6378.
33 C. P. Deck and K. Vecchio, *Carbon*, 2006, **44**, 267–275.
34 Z. M. Zhu, T. L. Chen, Y. Gu, J. Warren and R. M. Osgood, *Chem. Mater.*, 2005, **17**, 4227–4234.
35 R. Loukrakpam, J. Luo, T. He, Y. S. Chen, Z. C. Xu, P. N. Njoki, B. N. Wanjala, B. Fang, D. Mott, J. Yin, J. Klar, B. Powell and C. J. Zhong, *J. Phys. Chem. C*, 2011, **115**, 1682–1694.
36 W. Z. Li and P. Haldar, *Electrochem. Solid-State Lett.*, 2010, **13**, B47–B49.
37 F. Hasche, M. Oezaslan and P. Strasser, *J. Electrochem. Soc.*, 2012, **159**, B25–B34.
38 S. J. Bae, S. J. Yoo, Y. Lim, S. Kim, Y. Lim, J. Choi, K. S. Nahm, S. J. Hwang, T. H. Lim, S. K. Kim and P. Kim, *J. Mater. Chem.*, 2012, **22**, 8820–8825.
39 K. A. Kuttiyiel, K. Sasaki, Y. M. Choi, D. Su, P. Liu and R. R. Adzic, *Nano Lett.*, 2012, **12**, 6266–6271.
40 S.-I. Choi, S. Xie, M. Shao, J. H. Odell, N. Lu, H.-C. Peng, L. Protsailo, S. Guerrero, J. Park, X. Xia, J. Wang, M. J. Kim and Y. Xia, *Nano Lett.*, 2013, **13**, 3420–3425.
41 B. Lim, M. J. Jiang, P. H. C. Camargo, E. C. Cho, J. Tao, X. M. Lu, Y. M. Zhu and Y. N. Xia, *Science*, 2009, **324**, 1302–1305.
42 X. G. Li, S. Park and B. N. Popov, *J. Power Sources*, 2010, **195**, 445–452.
43 C. Koenigsmann, E. Sutter, T. A. Chiesa, R. R. Adzic and S. S. Wong, *Nano Lett.*, 2012, **12**, 2013–2020.
44 S. M. Alia, K. O. Jensen, B. S. Pivovar and Y. S. Yan, *ACS Catal.*, 2012, **2**, 858–863.
45 K. Jayasayee, J. A. R. Van Veen, T. G. Manivasagam, S. Celebi, E. J. M. Hensen and F. A. de Bruijn, *Appl. Catal., B*, 2012, **111**, 515–526.
46 A. Marcu, G. Toth, R. Srivastava and P. Strasser, *J. Power Sources*, 2012, **208**, 288–295.
47 H. Y. Park, T. Y. Jeon, J. H. Jang, S. J. Yoo, K. H. Choi, N. Jung, Y. H. Chung, M. Ahn, Y. H. Cho, K. S. Lee and Y. E. Sung, *Appl. Catal., B*, 2013, **129**, 375–381.
48 Z. Y. Zhang, M. J. Li, Z. L. Wu and W. Z. Li, *Nanotechnology*, 2011, **22**, 015602.

